Metal nanoparticle assembly with broadband absorption and suppressed thermal radiation for enhanced solar steam generation

ARTICLE

Metal nanoparticle assembly with broadband absorption and suppressed thermal radiation for enhanced solar steam generation

Dawei Ding,*[a] Hu Wu,[a] Xiaoping He,[a] Fan Yang,[c] Chuanbo Gao,*[b] Yadong Yin[c] and Shujiang Ding*[a]

Solar steam generation is an attractive technology for harvesting solar energy. Many efforts have been devoted to developing absorbers with increased solar energy absorption efficiency. However, little attention has been paid to the thermal radiation loss of the absorbers, which is equally important for achieving a high solar-steam efficiency. To address this issue, herein, we report a solar harvesting strategy by introducing a nickel-nanoparticle-based spectrally selective absorber that possesses high and broadband absorption in the solar irradiation region but minimal thermal emittance at long-infrared wavelengths. Nickel nanoparticles are encapsulated in silica and carbon nanoshells, which are then orderly assembled on an infrared reflector to form a harvesting structure of graded refractive indices. As a result, a high solar absorptance ($\alpha \approx 0.93$) but a low thermal emittance ($\varepsilon \approx 0.096$) have been achieved. An interfacial evaporation system with this unique absorber demonstrates a boosted water evaporation rate of 1.52 kg·m^{-2}· h^{-1} under 1 sun, which is ~ 5 times the value of water only, making it one of the best absorbers for the solar steam generation application. The combined advantages of high efficiency and durability suggest its potential for industrial water purification and desalination applications.

Introduction

Solar-thermal technology has been developed for many applications owing to its high conversion efficiency among the current solar technologies.[1-4] Solar-driven water evaporation, a direct way of harvesting solar-thermal energy to generate steam, has been the subject of scientific research and industrial efforts in the past decades.[5-8] The current challenge in solar water evaporation is to develop cost-efficient techniques that can realize high flux steam generation at a high conversion efficiency under one sun (1 kW·m^{-2}). An effective approach is to confine the heat at the evaporation surface of the water, known as interfacial evaporation, which prevents massive loss of heat during its transfer from the heat generation sites to the evaporation surface.[9-13] The localized water evaporation strategy has shown significantly improved evaporation efficiency compared with conventional water evaporation systems such as solar still or volumetric heating.[14-16]

To achieve highly efficient interfacial evaporation, a lot of efforts have been made to improve the evaporation system, including using black absorbers to maximize the absorption of the broad-spectrum solar energy, and constructing hierarchical porous nanostructures to facilitate water transportation and evaporation.[17-23] However, little attention has been paid to the thermal radiation loss of the absorbers. So far, the majority of solar absorbers developed for the interfacial evaporation systems are ultra-black materials. These ultra-black absorbers, exhibiting high absorption at wide-range wavelengths covering the full solar spectrum (0.25–2.5 µm) and the long-wavelength infrared region (2.5–25 µm), absorb solar energy and simultaneously lose heat via thermal radiation in the infrared region as a blackbody, according to Kirchhoff's law. Taking a blackbody absorber working at T = 100 °C, the boiling point of water at ambient conditions, for example, the thermal radiation loss to the ambient (T = 20 °C) can reach up to 680 W·m^{-2}, which accounts for 68% of the incident solar energy (AM 1.5). Even at a lower temperature of T = 50 °C, the thermal radiation loss can still be as high as 200 W·m^{-2}. It is expected that the solar-thermal output for the water evaporation could be further improved substantially by reducing the parasitic thermal radiation loss of the absorbers.

Here, we propose a rationally designed solar harvesting model to demonstrate the advantages of combining broadband absorption and suppressed thermal radiation in achieving a high solar steam efficiency. A solar-thermal conversion platform with nickel nanoparticle (Ni NP)-based spectrally selective solar absorbers (SSA-Ni) was developed for the interfacial water evaporation. Ni NPs were first encapsulated in carbon and silica

[a.] School of Chemistry, State Key Laboratory of Electrical Insulation and Power Equipment, Xi'an Jiaotong University, Xi'an, Shaanxi 710049, China. Emails: davidding1@mail.xjtu.edu.cn (D.D.); dingsj@mail.xjtu.edu.cn (S.D.)

[b.] Center for Materials Chemistry, Frontier Institute of Science and Technology, and State Key Laboratory of Multiphase Flow in Power Engineering, Xi'an Jiaotong University, Xi'an, Shaanxi 710054, China. Email: gaochuanbo@mail.xjtu.edu.cn (C.G.).

[c.] Department of Chemistry, University of California, Riverside, California 92521, United States.

shells and then orderly assembled to form a solar harvesting structure of graded refractive indices on an infrared reflector. This configuration realizes a high solar absorptance ($\alpha \approx 0.93$) and low thermal emittance ($\varepsilon \approx 0.096$). As a result, a high evaporation rate of 1.52 kg·m^{-2}·h^{-1} was achieved for the floating evaporation system with the SSA-Ni film under one sun, which is ~ 5 times the value of the pure water. We also demonstrate the excellent durability and desalination effect of the floating evaporation system under outdoor non-ideal weather conditions, which indicates its great potential in practical applications.

Experimental

Synthetic procedures

Synthesis of the SSA-Ni film: Ni NPs and Ni@SiO$_2$ NPs were prepared following our previously reported method.[24] Briefly, in a well-mixed Ni growth solution of SDS (0.01 M), oleic acid (10^{-4} M), and 10 mL of NiNO$_3$·6H$_2$O (10^{-3} M), fresh NaBH$_4$ was added to give a black color mixture. After 1h, Ni NPs were centrifuged and dispersed in 10 mL of H$_2$O. Before SiO$_2$ coating, Ni NPs were modified by incorporating 2 mL of PVP (10K, 5wt %) and were vortexed for 30 min, then centrifuged and dispersed in 12 mL of H$_2$O. The above Ni NPs were injected into 80 mL of ethanol, sonicated, and then 2 ~ 3 mL of Diethylamine (DEA), and 0.6 mL of TEOs were added quickly. After 60 min, the Ni@SiO$_2$ NPs were centrifuged and washed. Ni@RF NPs were synthesized by mixing the Ni NPs, 28 µL of formaldehyde, and 20 mg of resorcinol in 28 mL of H$_2$O, stirred, and then 100 µL of diluted ammonia (2.8%) was added. The mixture was placed in a round-bottom flask and refluxed at 50 °C for 2h, then cooled down, centrifuged, and washed. The SSA-Ni film was prepared on a metal mesh by dip-coating and post-annealing treatment. Briefly, the synthesized Ni@SiO$_2$ and Ni@RF NPs were dispersed in 20 mL of ethanol, respectively. Then, 100 µL of Ni@RF NPs sol-gel was dipped onto a metal mesh (stainless steel, 2400 mesh), dried at 60 °C and this procedure was repeated 10 times to prepare the Ni@C absorbing layer. The top absorbing layer of Ni@SiO$_2$ was prepared through the same procedure. The coated metal mesh was then annealed at 650 °C for 4h at a heating rate of 5 °C min^{-1} under N$_2$ atmosphere.

Synthesis of rGO aerogel: The rGO aerogel was synthesized from GO using the frozen-drying method. GO powders (purchased from Aladdin Co.) were dispersed in H$_2$O with a concentration of 10 mg mL^{-1}, and then frozen-dried for 24 h to given brownish porous pallet. The GO aerogel was placed in a tube furnace and heated to 450 °C for 2 h under N$_2$ atmosphere to produce the rGO aerogel (rGO-ag). The purchased carbon fiber (CF) (hydrophilic, WOS 1009, thickness: 0.33 mm, CeTech Co. Ltd, China) was ultrasonically cleaned for use without any further treatment.

Characterization

The morphologies and structures of the samples were characterized by Field emission scanning electron microscopy (Gemini SEM 500, ZEISS) and Transmission electron microscopy (HT-7700, Hitachi). XRD tests were performed with a SmartLab X-ray diffraction (Rigaku, Japan). Raman spectra were collected using a Laser Raman Spectrometer equipped with a 532 nm laser. The optical diffuse reflectance spectra of the samples were recorded with a PerkinElmer Lambda 950 UV-Vis-NIR spectrophotometer in the range of $0.3 - 2.5$ µm and a Nicolet 6700 IR spectrophotometer in the range of $2.5 - 17$ µm equipped with an integrating sphere. Infrared photographs were taken by an Infrared camera (FLIR One).

Solar Steam Generation and Desalination Experiment

The steam generation experiments were performed under a solar simulator (Beijing optical century instrument) with a light spot size of 2 cm at a solar density of 100 mW·cm^{-2}. The experiments were typically conducted at an ambient temperature of 22 ± 1 °C and humidity of 50 ± 2%. The test chamber was a glass container (2 mm inner diameter and 34 mm height). In the experiment, the solar absorber (diameter = 2 cm) was supported by a polystyrene (height = 8 mm) with a tiny pore filled with hydrophilic fiber as water channels and was floating on the surface of the water in the chamber. The mass change was measured and recorded by a high accuracy balance for the evaluation of the evaporation rate and solar water evaporation efficiency. The amount of Ni in water after the stability test was examined by ICP-MS (NexIONTM 350D, PerkinElmer). To demonstrate the solar desalination capability of the SSA-Ni evaporator, a prototype solar water purification device simulating a practical solar water purification equipment was built. A SSA-Ni evaporator (diameter = 4 cm) was placed in a transparent condenser with a continuous supply of brine from a brine tank. The brine sample with representative simulated salinities of World sea (average salinity, 35‰) was used and the water quality of purified water was evaluated by the conductivity value.

Results and discussion

A floating evaporation device of the SSA-Ni film and polystyrene foam was designed as shown in Fig. 1a. Water was pumped to the heated zone of SSA-Ni film through the water channel in the polystyrene foam and vaporizes locally. We took advantage of the broadband optical excitation of Ni NPs in the construction of the spectrally selective solar absorber. Unlike the plasmonic absorption mechanism, interband transitions can be excited by photons with the energy that surpasses the interband threshold of a metal, which makes some transition metals (e.g., Ni and Pt) with a high density of electronic states near their Fermi levels suitable for broadband solar energy utilization.[25] The high solar absorptance and spectral selectivity of SSA-Ni film were realized by nanostructure engineering. Ni NPs were synthesized and individually encapsulated into protective shells through a wet-chemistry method. The merit of this synthesis strategy is to enable Ni NPs size control and flexible function tuning of coated materials. Specifically, Ni NPs coated with silica (Ni@SiO$_2$), a dense layer of ceramic, which not only protected the particles against sintering, oxidation, and etching but also effectively reduced the reflection of incident light on the Ni NPs. Ni@SiO$_2$ NPs were used in constructing the first absorbing layer on top, with the carbon-coated Ni NPs (Ni@C) for the second layer due to its higher refractive index.
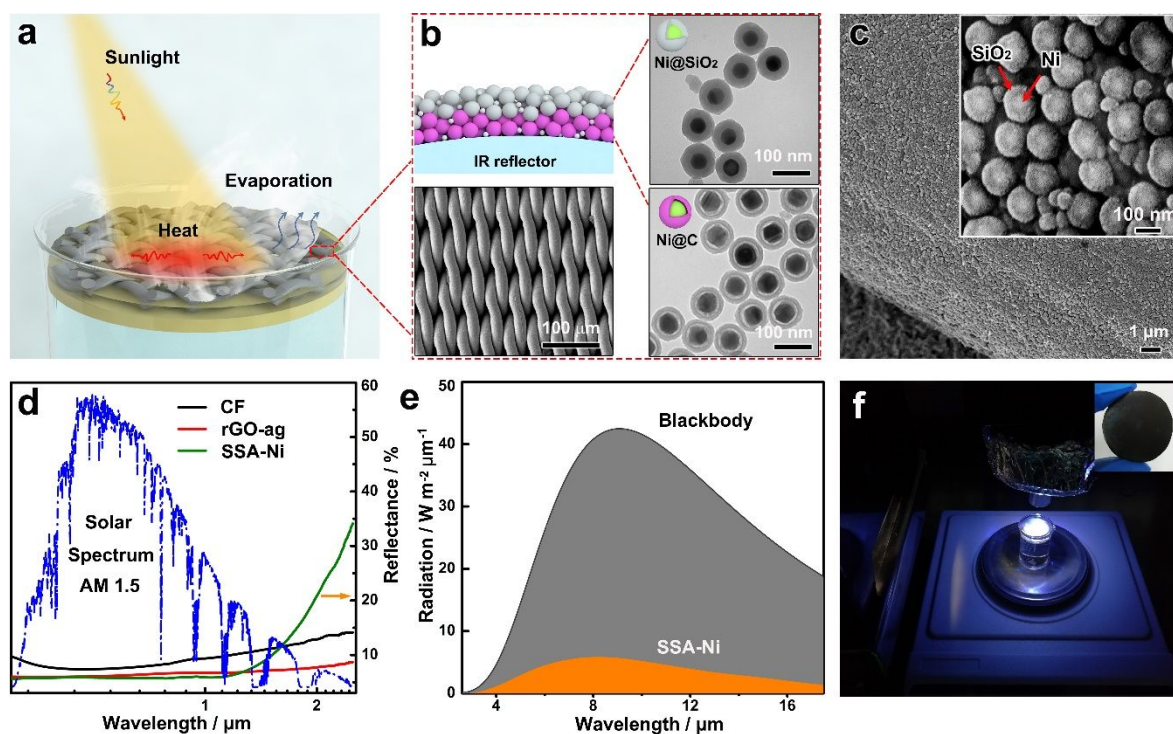
Fig. 1 SSA-Ni steam generation system. (a) Schematic illustration of the SSA steam generation system. Structure and composition of SSA-Ni film (b) and magnified microstructure of individual metal wire coated with Ni@SiO2 and Ni@C NPs (c). (d) UV-Vis-NIR spectra of the SSA-Ni film. The normalized spectral solar irradiance density (AM 1.5) is shown by the blue dash line. (e) Spectral thermal radiation loss of blackbody and SSA-Ni film at 46 °C, the working temperature in this study. (f) Photograph of the water evaporation system (Insert is the SSA-Ni sample).

The absorbing layers of graded refractive indices (low to high) could significantly reduce reflection in the main solar irradiation region and meanwhile enhance the absorption selectivity (Fig. 1b and Fig. S1, ESI†). These graded absorbing layers were orderly deposited on a metal substrate of high infrared reflection to further enhance its absorption selectivity. The obtained SSA-Ni film is shown in Fig. 1c. After layer-by-layer dip-coating and post-annealing treatment, it was revealed that the Ni@SiO$_2$ and Ni@C core-shell structures were well preserved during the deposition process (Fig. 1b and 1c). The XRD pattern of the as-prepared SSA-Ni film showed a sharp peak of Ni, confirming the crystallinity of Ni NPs. Furthers, the Raman spectrum confirmed the presence of carbonaceous components in the Ni@C NPs (Fig. S2, ESI†). The metal mesh substrate was uniformly covered with the absorbing layers and maintained its original structure (Fig. S3, ESI†).

For the solar-driven water evaporation operated at lower or near 100 °C, the ideal solar absorber is expected to exhibit low reflectivity (high absorptivity) in the wavelength of 0.25–2.5 μm and high reflectivity (low absorptivity) in the long-wavelength infrared region (2.5–25 μm) with a sharp transition since the peak of blackbody irradiation at 100 °C locates at the wavelength of ~8 μm. The optical properties of SSA-Ni film were tailored by controlling the composition of absorbing layers, layer thickness, as well as metal substrate. As a double-layer absorbing structure, the orderly assemble of two thin layers from surface to bottom improved light absorption by further reducing reflectivity in the visible and near-infrared region, meanwhile exhibited high reflectivity in the infrared region

owing to the high reflective metal substrate. The cut-off wavelength of light absorption can be either red-shifted or blue-shifted by changing the layer thickness.[26] As a result, reflectivity as low as 5% was realized for the optimized SSA-Ni film in the visible-to-near infrared region of the solar spectrum (Fig. 1d), which increased rapidly at wavelengths above 2.0 μm and maintained a high level (> 90%) in the long-wavelength infrared region (Fig. S4, ESI†). We also studied the optical properties of commercially available carbon fiber cloth (CF, thickness: ~0.3 mm) and the synthesized reduced graphene oxide aerogel (rGO-ag, thickness: ~3 mm, Fig. S5, ESI†). Both black-carbon absorbers exhibited good solar harvesting ability, of which the rGO-ag showed comparable low reflection as the SSA-Ni film and even lower in the wavelength of the near-infrared region. In the long-wavelength infrared region, the rGO-ag exhibited similar low reflectivity of a blackbody absorber (Fig. 1d and Fig. S4, ESI†). The high absorptivity in the long-wavelength infrared region resulted in a significant increase in thermal radiation. Assuming a blackbody absorber at T = 46 °C, the working temperature of the absorber in this study, the thermal radiation loss to the ambient (T = 22 °C) can be ~ 158 W·m^{-2}, accounting for 15.8 % of the incident solar energy (AM 1.5). For the rGO-ag absorber, the calculated radiation loss was close to the value of the blackbody absorber (S1.1 and Fig. S6, ESI†). In contrast, the SSA-Ni film of low thermal emittance (ε ≈ 0.093) was able to suppress over 90% of the thermal radiation loss (Fig. 1e), ensuring substantial enhancement of heat output for water evaporation. The photothermal properties of these two different kinds of absorbers were also tested under 1 sun
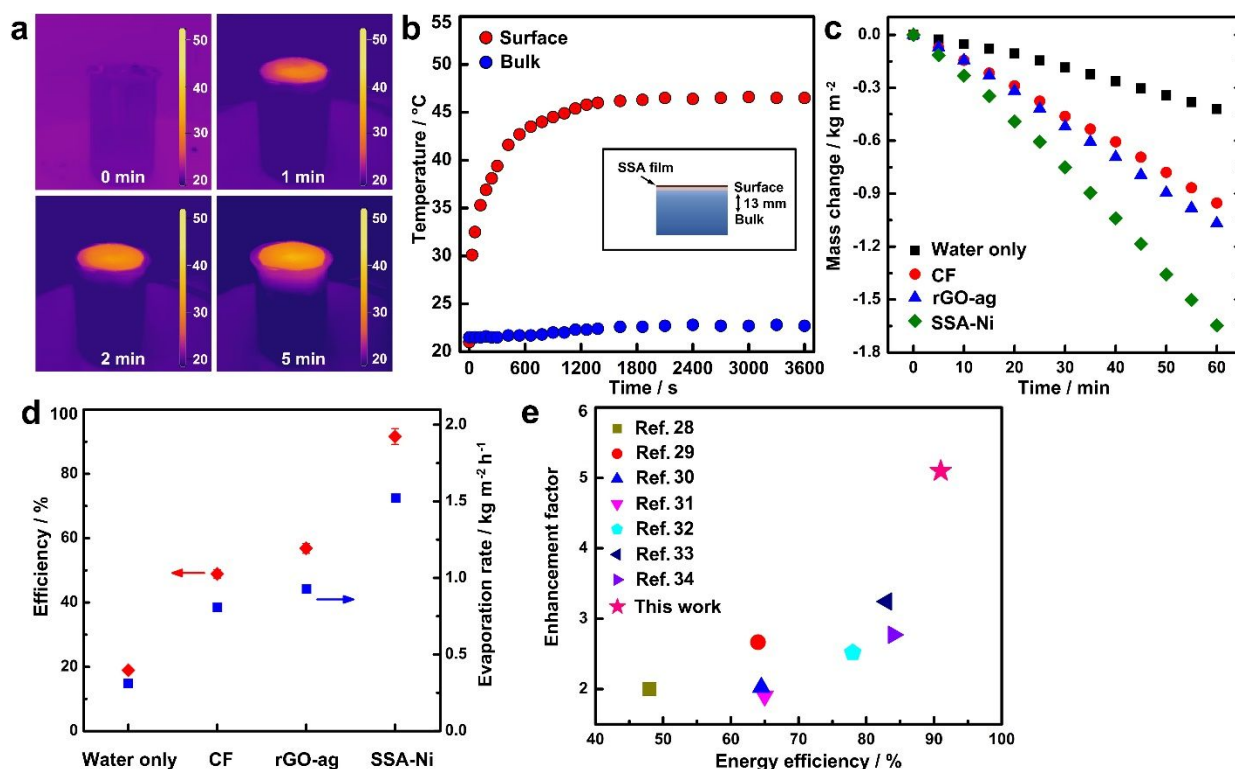
Fig. 2 Solar water evaporation performance under one sun (1 kW m-2). (a) IR pictures of the SSA-Ni film at the beginning of 5 min. (b) Surface, and bulk water temperatures of the SSA-Ni film as a function of time. (c) The mass change of water with and without different solar absorbers over time (ambient temperature: 22 ± 1 °C, humidity: 50 ± 2%). (d) Solar steam efficiency (circle, left-hand side axis) and evaporation rate (square, right-hand side axis) with different absorbers. (e) Comparison of water evaporation performance between SSA-Ni and previously reported typical materials of high solar absorption under 1 sun.

irradiation. The equilibrium temperature of the SSA-Ni reached 62.4 °C compared to 53.3°C for the blackbody absorber, demonstrating higher photothermal conversation efficiency of the SSA-Ni film than the blackbody absorber (Fig.S7, ESI†). It worth noting that the SSA-Ni film was not fully immersed in water, leaving the top surface exposed to the air to enable the heat localization at the water/air interface. Therefore, the thermal radiation loss mainly comes from the low thermal emissivity material itself.

A floating evaporation structure was prepared by placing the solar absorber on commercially available polystyrene foam with a tiny pore filled with hydrophilic fiber as water channels. The evaporation performance was demonstrated in lab-scale open water contained in a beaker under simulated one sun illumination (1 kW·m^{-2}), as shown in Fig. 1f. The temperature distribution in the evaporation system was studied by an IR camera. At the beginning of irradiation, the heated zone was confined within the surface of SSA-Ni film, which led to a sharp increase of temperature to 30 °C within 30 seconds, owing to the high solar-thermal conversion efficiency of SSA-Ni film (Fig. 2a and 2b). The surface temperature reached a plateau of ~ 46 °C when the equilibrium between heating and evaporation was reached. It was observed that the bulk water was heated at a much slower rate from the distribution of temperatures in the water container, owing to the low thermal conductivity of the polystyrene foam.

The evaporation rates of water with the SSA-Ni film and black carbon absorbers were measured by the weight change as a function of time, with pure water as the control. In a dark environment, the water evaporation rates were 0.15, 0.16, 0.16, and 0.20 kg·m^{-2}·h^{-1} for pure water, SSA-Ni, CF, and rGO-ag, respectively (Fig. S8, ESI†). The notable mismatch of water evaporation rate between rGO-ag and others may be caused by more evaporation surface areas and the reduced latent heat of water evaporation in the porous skeleton of rGO-ag.[27] In the calculation of the evaporation rate, the dark evaporation rate was subtracted from all the measured evaporation rates under solar illumination to isolate the effect of solar-driven water evaporation. The time-dependent mass change curves of different evaporation systems were shown in Fig. 2c. After an initial transient period, the evaporation rate reached a steady-state and can be calculated from the slope of the curve. For pure water, the evaporation rate was 0.31 kg·m^{-2}·h^{-1}. The evaporation rates increased obviously with the addition of solar absorber, to 0.80, 0.93, and 1.52 kg·m^{-2}·h^{-1} for CF, rGO-ag, and SSA-Ni film, respectively (Fig. 2d). Of all the water evaporation systems, the SSA-Ni exhibited the highest solar water evaporation rate, which was 4 times higher than pure water at 1 kW·m^{-2} illumination. The corresponding energy efficiency (η) for solar-to-vapor generation was defined as η = mh_v/q_{in}, where m is the mass flux, h_v denotes the water vaporization enthalpy, q_{in} is the power density of solar irradiation. The SSA-Ni evaporation system showed an outstanding energy efficiency of nearly 91%. The heat loss due to radiation, conduction, and convection was calculated to be 1.5%, ~3.6%, and ~6.0%, respectively (S1.2, ESI†). There is a mismatch between the total energy loss of ~11.1% and the water-to-vapor efficiency (~ 91%), which can be attributed to deviations in the theoretical
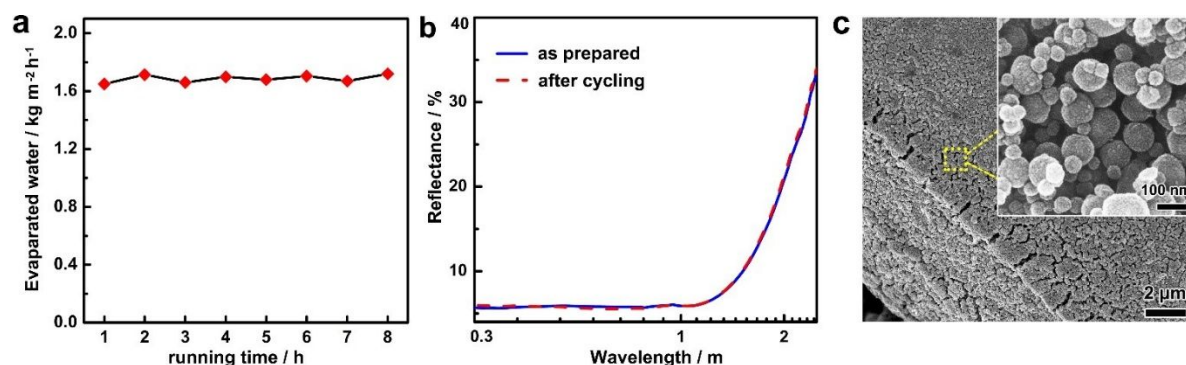
Fig. 3 Stability performance. (a) the water evaporation cycling performance of the SSA-Ni. (b) the optical and (c) morphology characterization of the SSA-Ni after cycling test.

and empirical data of water vaporization enthalpy, convection heat transfer coefficient, etc., in the calculation of the energy efficiency and the heat loss.

We also compare the SSA-Ni film of this work with the state-of-art solar absorbers for interfacial water evaporation reported recently. It's worth noting that since the water evaporations were done under different conditions, including surrounding temperature, humidity, light source, etc., it is difficult to directly compare the solar steam performances of various materials by water evaporation rates (Table S1, ESI†). In this regard, the enhancement factor, defined as the ratio of the evaporation rates with solar absorbers versus pure water, is more appropriate than water evaporation rates in characterizing the efficiency of a solar-driven evaporation system. As plotted in Fig. 2e, an enhancement factor of up to 5 was achieved for the SSA-Ni film in this work, making it one of the best solar absorbers, including carbon-based as well as

plasmonic-based absorbing materials as reported, of which the enhancement factors are usually lower than 3.[28-34] The superior solar-to-steam performance of the SSA-Ni film to the aforementioned materials relies on its ability of efficient absorption of the broad-spectrum solar radiation and simultaneous suppression of thermal radiation loss.

The stability of SSA-Ni film during long-term solar water evaporation was investigated. It was shown that the mass change of evaporated water was maintained at a stable value of ~ 1.68 kg·m^{-2}·h^{-1} during the cycling (Fig. 3a). Freshwater was supplied every two-hour, which could cause a slight mass drop. The stability of SSA-Ni film was further investigated by optical, morphological, and structural characterization. It was clearly shown that the reflecting curves of the absorber before and after cycling barely changed. The SEM image of the SSA-Ni film after the cycling showed that the core/shell structure, Ni@SiO$_2$, and Ni@C nanoparticles were well-preserved (Fig. 3b and 3c);
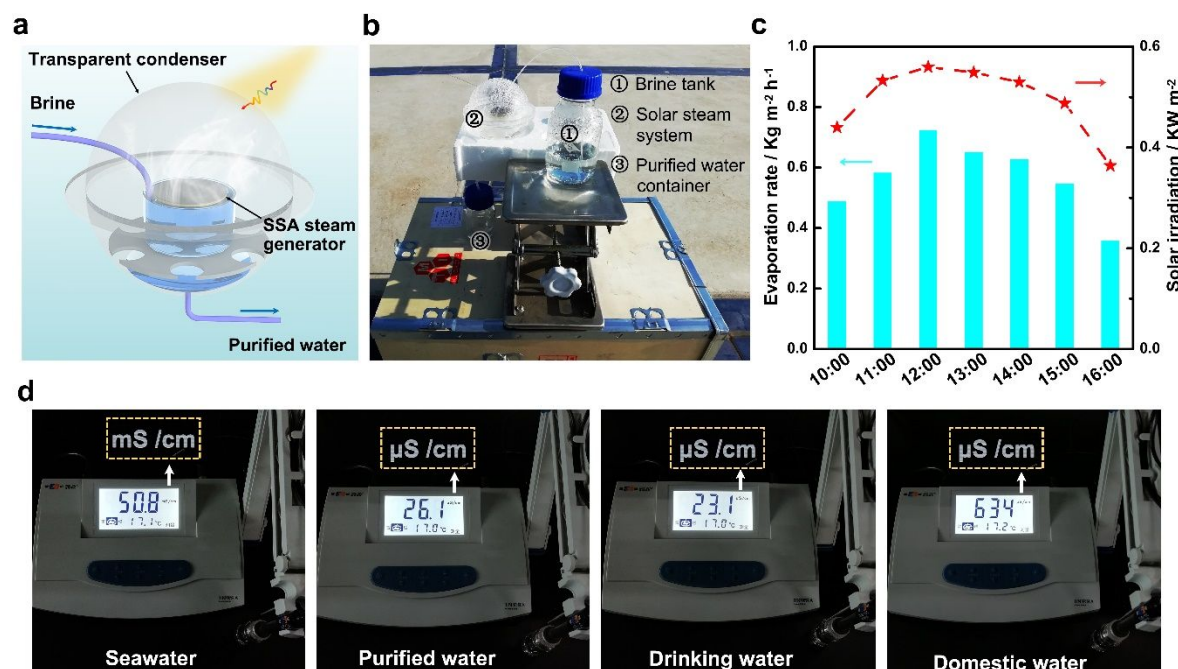

Fig. 4 Outdoor solar water purification using SSA-Ni in natural sunlight. Schematic illustration of water collector (a) for a prototype solar water purification equipment based on SSA-Ni (b). (c) The steam-generation performance of the solar desalination device based on SSA-Ni in natural sunlight at different times within one day. Note: The experiments were done at XJTU Innovation Harbor (Xi'an, Shaanxi, China) on November 7, 2020. d, Evaluation of water purity by measuring conductivity values.

no chemical changes were observed for the nanoparticle-based absorber, indicating the good stability of the materials (Figure S2, ESI†). After the stability test, the content of Ni in water was monitored, and a trace amount of Ni (0.055 mg L^{-1}) was detected, indicating the improved stability of the nanoparticles. The SSA-Ni evaporation system also exhibited stable steam generation performance in artificial seawater; no obvious decay in evaporation rate after six cycles of test, nor during 8 h of continuous evaporation was observed (Fig. S9, ESI†).

To demonstrate the practical solar desalination capability of the SSA-Ni film, simulated seawater of world sea (average salinity, 35‰) with four primary ions (Na$^+$, Mg^{2+}, K$^+$, and Ca^{2+}) was used for evaporation. A prototype solar water purification equipment based on the SSA-Ni film was built and placed on the roof of the lab building (Fig. 4a and 4b). Here, an SSA-Ni film with a diameter of ~4 cm was floated in a brine container, which was placed in a transparent condenser. The brine was continuously supplied by a brine tank, and the purified water was collected through a pipe to a water container. The experiment was carried out from 10:00 to 16:00 under natural sunlight with an average solar flux of 0.5 KW· m^{-2}. The solar irradiation density, ambient temperatures, and humidity were traced to evaluate the utilization efficiency of natural sunlight (Fig. 4c and Fig. S10, ESI†). The SSA-Ni evaporator demonstrated excellent water purification capability even under non-ideal conditions, with an evaporation rate of 0.73 kg·m^{-2}·h^{-1} at a maximum solar flux of ~ 0.56 KW·m^{-2}, revealing its significant potential for practical applications. The quality of the purified water was directly evaluated by measuring the conductivity value (Fig. 4d). The seawater, purified water, drinking water (from a local bottled purified drinking water supplier), and domestic water (from the urban water-supply system) showed conductivity values of 50.8, ~ 0.026, ~ 0.023 and ~ 0.63 mS·cm^{-1}, respectively, indicating effective purification of the seawater.

Conclusions

In summary, we present an efficient solar steam generation system by integrating highly efficient solar-thermal conversion materials and the interfacial evaporation strategy. The SSA-Ni solar-thermal conversion film simultaneously realized high solar absorptance and low thermal emittance, resulting in much improved solar-thermal conversion efficiency. A high solar vapor efficiency of ~ 91% at an evaporation rate of 1.52 kg·m^{-2}·h^{-1} under 1 sun was achieved in this work, with an enhancement factor of up to 5 versus pure water. Besides, the SSA-Ni evaporator also demonstrated excellent outdoor desalination performance in natural sunlight. This work provides the rational design of a solar-thermal conversion platform for interfacial water evaporation. The combination of broadband absorption and suppressed thermal radiation ensures a high energy utilization efficiency. The reported strategy can be readily used in practical applications such as large-scale steam generation, water purification, and seawater desalination.

Conflicts of interest

There are no conflicts to declare.

Acknowledgements

Notes and references

1 S. D. Tilley, *Adv. Energy Mater.*, 2019, **9**, 1802877.
2 M. Gao, L. Zhu, C. K. Peh and G. W. Ho, *Energ. Environ. Sci.*, 2019, **12**, 841.
3 T. Leijtens, K. A. Bush, R. Prasanna and M. D. McGehee, *Nat. Energy*, 2018, **3**, 828.
4 H. Ren, M. Tang, B. Guan, K. Wang, J. Yang, F. Wang, M. Wang, J. Shan, Z. Chen, D. Wei, H. Peng and Z. Liu, *Adv. Mater.*, 2017, **29**, 1702590.
5 Z. Xu, L. Zhang, L. Zhao, B. Li, B. Bhatia, C. Wang, K. L. Wilke, Y. Song, O. Labban, J. H. Lienhard, R. Wang and E. N. Wang, *Energ. Environ. Sci.*, 2020, **13**, 830.
6 Z. Wang, C. Li and K. Domen, *Chem. Soc. Rev.*, 2019, **48**, 2109.
7 Q. Ma, P. Yin, M. Zhao, Z. Luo, Y. Huang, Q. He, Y. Yu, Z. Liu, Z. Hu, B. Chen and H. Zhang, *Adv. Mater.*, 2019, **31**, 1808249.
8 C. Li, Y. Goswami and E. Stefanakos, *Renew. Sust. Energ. Rev.*, 2013, **19**, 136.
9 F. Zhao, Y. Guo, X. Zhou, W. Shi and G. Yu, *Nat. Rev. Mater.*, 2020, **5**, 388.
10 L. Zhou, Y. Tan, J. Wang, W. Xu, Y. Yuan, W. Cai, S. Zhu and J. Zhu, *Nat. Photonics*, 2016, **10**, 393.
11 Y. Liu, S. Yu, R. Feng, A. Bernard, Y. Liu, Y. Zhang, H. Duan, W. Shang, P. Tao, C. Song and T. Deng, *Adv. Mater.*, 2015, **27**, 2768.
12 Y. Ito, Y. Tanabe, J. Han, T. Fujita, K. Tanigaki and M. Chen, *Adv. Mater.*, 2015, **27**, 4302-4307.
13 Z. Wang, Y. Liu, P. Tao, Q. Shen, N. Yi, F. Zhang, Q. Liu, C. Song, D. Zhang, W. Shang and T. Deng, *Small*, 2014, **10**, 3234.
14 G. Ni, N. Miljkovic, H. Ghasemi, X. Huang, S. V. Boriskina, C.-T. Lin, J. Wang, Y. Xu, M. M. Rahman, T. Zhang and G. Chen, *Nano Energy*, 2015, **17**, 290.
15 G. Xiao, X. Wang, M. Ni, F. Wang, W. Zhu, Z. Luo and K. Cen, *Appl. Energ.*, 2013, **103**, 642.
16 O. Neumann, A. S. Urban, J. Day, S. Lal, P. Nordlander and N. J. Halas, *ACS Nano*, 2013, **7**, 42.
17 C. Chen, Y. Kuang, L. Hu, *Joule*, 2019, **3**, 683.
18 Y. Yang, R. Zhao, T. Zhang, K. Zhao, P. Xiao, Y. Ma, P.M. Ajayan, G. Shi, Y. Chen, *ACS Nano*, 2018, **12**, 829.
19 F. Zhao, X. Zhou, Y. Shi, X. Qian, M. Alexander, X. Zhao, S. Mendez, R. Yang, L. Qu, G. Yu, *Nat. Nanotechnol.*, 2018, **13**, 489.
20 P. Tao, G. Ni, C. Song, W. Shang, J. Wu, J. Zhu, G. Chen and T. Deng, *Nat. Energy*, 2018, **3**, 1031.
21 M. Zhu, Y. Li, F. Chen, X. Zhu, J. Dai, Y. Li, Z. Yang, X. Yan, J. Song, Y. Wang, E. Hitz, W. Luo, M. Lu, B. Yang, L. Hu, *Adv. Energy Mater.*, 2018, **8**, 1701028.

22 J. Wang, Y. Li, L. Deng, N. Wei, Y. Weng, S. Dong, D. Qi, J. Qiu, X. Chen, T. Wu, *Adv. Mater.*, 2017, **29**, 1603730.
23 X. Li, W. Xu, M. Tang, L. Zhou, B. Zhu, S. Zhu, J. Zhu, *P. Natl. Acad. Sci., U.S.A.*, 2016, **113**, 13953.
24 D. Ding, K. Liu, Q. Fan, B. Dong, Y. Zhang, Y. Yin, C. Gao and S. Ding, *J. Mater. Chem. A*, 2019, **7**, 3039.
25 Y. Yuan, C. Dong, J. Gu, Q. Liu, J. Xu, C. Zhou, G. Song, W. Chen, L. Yao, D. Zhang, *Adv. Mater.*, 2020, **32**, 1907975.
26 D. Ding, W. Cai, M. Long, H. Wu, Y. Wu, *Sol. Energ. Mat. Sol. C.*, 2010, **94**, 1578.
27 B. Bellich, M. Borgogna, M. Cok and A. Cesaro, *J. Therm. Anal. Calorim.*, 2011, **103**, 81.
28 L. Zhou, S. Zhuang, C. He, Y. Tan, Z. Wang and J. Zhu, *Nano Energy*, 2017, **32**, 195.
29 H. Ghasemi, G. Ni, A. M. Marconnet, J. Loomis, S. Yerci, N. Miljkovic and G. Chen, *Nat. Commun.*, 2014, **5**, 4449.
30 L. Yi, S. Ci, S. Luo, P. Shao, Y. Hou and Z. Wen, *Nano Energy*, 2017, **41**, 600.
31 C. Chen, Y. Li, J. Song, Z. Yang, Y. Kuang, E. Hitz, C. Jia, A. Gong, F. Jiang, J. Y. Zhu, B. Yang, J. Xie and L. Hu, *Adv. Mater.*, 2017, **29**, 1701756.
32 X. Han, W. Wang, K. Zuo, L. Chen, L. Yuan, J. Liang, Q. Li, P. M. Ajayan, Y. Zhao and J. Lou, *Nano Energy*, 2019, **60**, 567.
33 X. Hu, W. Xu, L. Zhou, Y. Tan, Y. Wang, S. Zhu and J. Zhu, *Adv. Mater.*, 2017, **29**, 1604031.
34 R. Li, L. Zhang, L. Shi and P. Wang, *ACS Nano*, 2017, **11**, 3752.